Energy & Environmental Science

Unraveling the Core of Fuel Cell Performance: Engineering the Ionomer/Catalyst Interface

Journal:	*Energy & Environmental Science*
Manuscript ID	EE-ART-11-2022-003553.R3
Article Type:	Paper
Date Submitted by the Author:	07-May-2023
Complete List of Authors:	Li, Chenzhao; Purdue University, School of mechanical Engineering; Indiana University Purdue University at Indianapolis, Department of Mechanical and energy engineering Yu, Kang; Materials Science and Engineering Program, The University of Texas at Austin Bird, Ashley; Lawrence Berkeley National Laboratory Guo, Fei; University of California, Davis, Department of Molecular and Cellular Biology Ilavsky, Jan; Argonne National Laboratory Advanced Photon Source Liu, Yadong; Indiana University Purdue University at Indianapolis, Cullen, David; Oak Ridge National Laboratory, Materials Science & Technology Division Kusoglu, Ahmet; Lawrence Berkeley National Laboratory, Energy Storage and Distributed Resources; Lawrence Berkeley National Lab Weber, Adam; Lawrence Berkeley National Laboratory, Energy Technologies Area Fereira, Paulo; INL - International Iberian Nanotechnology Laboratory , International Iberian Nanotechnology Laboratory (INL); International Iberian Nanotechnology Laboratory (INL) Xie, Jian; Indiana University Purdue University at Indianapolis, Department of Mechanical Engineering

Novel concept. There have been many reported breakthroughs on novel and extremely high activity catalysts for fuel cells published on both *Nature* and *Science* (e.g. *Chen, et al*, ***SCIENCE,*** *343, 1339, 2014, and Huang, et al,* ***Science*** *348, 1230, 2015*), which based on their performance measured using the rotation disc electrode (RDE). However, these breakthroughs are rarely realized in a membrane electrode assembly (MEA), which is the core component of fuel cells and affects practical fuel cell development. Therefore, **the long-standing challenge is to bridge the gap between the catalyst RDE performance, and the effective MEA as pointed out by the recent review article published on *Nature Energy*** (*Fan et al*, "*Bridging the gap between highly active oxygen reduction reaction catalysts and effective catalyst layers for proton exchange membrane fuel cells*", *Nature Energy, 6, 475, (2021)*). It is the first time that we propose the concept that the ionomer/catalyst interface ultimately determines the performance of a membrane electrode assembly (MEA) (*Xie and Le et al, ECS 2016 Meet. Abstr.* **MA2016-02** 2584), consequently, the catalyst utilization and high current density performance-rated/peak power density. In this work, we also propose the concept of the ideal ionomer/catalyst interface and how to build such an ideal interface. Instead of the trail-error approach and many approaches focusing on individual aspect of a MEA, such as improving the ionomer oxygen permeability, pore structure, carbon hydrophobicity, catalyst accessibility, we report, for the first time, how to unlock the performance of a catalyst in the MEA by engineering the ionomer/catalyst interface where the ORR takes place. We take the rational approach of solving the longstanding PEMFC challenge of translating RDE performance into a MEA by designing the ideal ionomer/catalyst interface and achieving such an interface utilizing the electrostatic charge attraction in a liquid state. Simultaneously, we attack another longstanding challenge: imaging the ionomer/catalyst interface using TEM. To best of our knowledge, there has been no such concept being reported yet. As the result, the MEA with this new interface achieved >75% of catalyst RDE performance (*vs.* less than 45% in general) and the peak/rated power density (1.430 W/cm^2/0.930 W/cm^2, respectively for H_2/Air, Pt loading: 0.1 mg_{Pt}/cm^2 and 150 kPa absolute pressure) for pure Pt catalysts, even better than those of Pt alloy catalysts.

Significance. The MEA is the most important component in PEMFC. For the last three decades, guided by the multi-scale modeling work, great progress has been made for the catalyst research with many catalysts developed, which show the excellent catalytic activity for the oxygen reduction reaction (ORR) measured by the rotating disc electrode (RDE). However, a catalyst must be incorporated into the catalyst layer of a MEA for PEMFC applications. Yet, the catalyst RDE performance is rarely realized in the MEA, which is a long-standing challenge for PEMFC. Wilson and Gottesfeld from the Los Alamos National Laboratory revolutionized the MEA structure by introducing the ionomer into the catalyst layer to provide proton conduction in 1991 (**DOI**https://doi.org/10.1149/1.2069277), which tremendously reduced the Pt loading from 4-6 to 0.4 mg_{Pt}/cm^2 and thus, greatly improved the MEA performance. However, since then, the basic

MEA structure remains the same and there is no control of the ionomer distribution inside a catalyst layer, not even mentioning the formation of ionomer/catalyst interface. In addition, most of the MEA work uses the trial-error approach and very limited progress has been made. For the first time since 1991, we report a new design of the MEA structure using the concept of the ionomer/catalyst interface to overcome the long-standing challenges of PEMFC and boost the performance. We propose that the core of the MEA performance lies on the ionomer/catalyst interface, which is exactly where the ORR occurs. We designed/engineered the ideal ionomer/catalyst interface to realize such an interface utilizing the electrostatic charge attraction between negatively charged ionomer and positively charged catalyst particles to control the formation of the ionomer/catalyst interface over the surface of Pt catalyst nanoparticles (Fig 1). Such designed interface leads to the unprecedented MEA performance in terms of mass activity, ECSA, and rated/peak power density, exceeding all reported pure Pt/C catalyst MEAs on rated/peak power density, even matching that of Pt alloy catalysts. Such a new MEA also achieved >75% of catalyst RDE performance (*vs.* less than 45% in general). In addition, this approach can be directly applied for fabricating the high-performance MEA for PEMFCs, which will certainly accelerate the fuel cell electric vehicle (FCEV) massive commercialization. Finally, this approach demonstrates a method of solving the practical engineering challenge with a solid and fundamental understanding through establishing property (ink)-structure (interface)-performance relationship.

Broad impact. All of the work demonstrates that our design of the ideal ionomer/catalyst interface and the realization of such interface are essential for the ultimate fuel cell performance. Such a concept of the ideal interface is of paramount importance to all reactions involving the solid/gas/liquid interface, such as heterogonous catalysis (i.e., water electrolysis and electrolysis in alkali industry, etc.) and other applications (i.e., solid-state batteries, etc.). This opens a new avenue for developing highly efficient devices for energy conversion/storage (i.e., fuel cells, batteries), hydrogen production (i.e., water electrolysis) and other applications (i.e., alkaline industry). This work suggests that with a fundamental understanding of the challenges, solving the problem from the fundamentals of the interface of ionomer/catalyst, designing the ideal interface, and engineering to construct such interface based on the relationship of the property-structure-performance is an innovative approach for dealing with complicated challenges we are facing today.

We really hope that you and manuscript reviewers will find this manuscript of the highest interest and worthy publication in *Energy and Environmental Science*. This manuscript has not been submitted previously and is not under consideration for publication elsewhere.

Unraveling the Core of Fuel Cell Performance: Engineering the Ionomer/Catalyst Interface

Chenzhao Li [1,2], Kang Yu [3,4], Ashley Bird [5,6], Fei Guo [7], Jan Ilavsky [8], Yadong Liu [1], David A. Cullen [9], Ahmet Kusoglu [5], Adam Z. Weber [5], Paulo Ferreira [3,4,10], and Jian Xie [1, *]

[1]Department of Mechanical and Energy Engineering and Integrated Nanosystems Development Institute, Purdue School of Engineering and Technology, Indiana University-Purdue University, Indianapolis, Indiana 46202, USA

[2]School of Mechanical Engineering, Purdue University, West Lafayette, Indiana 47906, USA

[3]Materials Science and Engineering, University of Texas at Austin, Austin, TX, 78712, USA

[4]International Iberian Nanotechnology Laboratory, Braga, Portugal

[5]Energy Conversion Group, Energy Technologies Area, Lawrence Berkeley National Laboratory, Berkeley, California 94720, USA

[6]Department of Chemical and Biomolecular Engineering, University of California Berkeley, Berkeley, California 94720, USA

[7]Department of Molecular and Cellular Biology, University of California, Davis, Davis, CA 95616-8665, USA

[8]X-Ray Science Division, Argonne National Laboratory, Lemont, Illinois 60439, USA

[9]Center for Nanophase Materials Sciences, Oak Ridge National Laboratory, Oak Ridge, TN 37831, USA

[10]Mechanical Engineering Department and IDMEC, Instituto Superior Técnico, University of Lisbon, Av. Rovisco Pais, 1049-001 Lisboa, Portugal

*Correspondence: jianxie@iupui.edu;

ABSTRACT

The biggest obstacle to the widespread implantation of the polymer electrolyte membrane fuel cells (PEMFCs) is the cost, primarily due to the use of platinum catalysts. The high intrinsic catalyst activity exhibited on a rotating disk electrode (RDE) is rarely realized in the membrane electrode assembly (MEA), which is the long-standing challenge for PEMFC and causes the low catalyst utilization. To translate the high RDE performance of catalyst into MEA, the design of an ideal ionomer/catalyst interface is proposed: a thin, conformal ionomer film covers the maximum surface of a Pt nanoparticle and thus simultaneously maximizes catalyst utilization, (i.e., high mass activity and electrochemical active surface area) and O_2 diffusion rate (i.e., high current density performance) without compromising proton conduction. Building such an interface is a long-standing challenge due to the lack of the interaction between the ionomer and catalyst particles, resulting in large ionomer agglomerates and inhomogeneous ionomer coverage over the catalyst nanoparticle, consequently, poor fuel cell performance. In this work, this ionomer/catalyst interface has been engineered utilizing the electrostatic attraction between positively charged catalyst and negatively charged ionomer particles in a catalyst ink and preserved into a solid catalyst layer. As the results, this interface leads to the previously unachieved proton exchange membrane fuel cell performance on both the catalyst utilization (75% vs. 45%) and the peak/rated power density (i.e., 1.430 /0.930 W/cm^2, H_2/Air, cathode Pt loading: 0.1 mg_{Pt}/cm^2) for pure Pt catalysts, even better than those of Pt alloy catalysts. This work demonstrated the formation of the interface in the liquid phase (using ultra-small angle -ray scattering in combination with cryo-TEM, isothermal-titration-calorimetry) and the preserved interface in the solid catalyst layer (using TEM) and estimated the effective coverage and the thickness of the ionomer film (using the limiting current density, RDE and fuel cell performance).

INTRODUCTION

With the surge of interest in electrification of transportation driven by global climate change, the need for the powertrains using non-carbon energy sources has become more urgent than ever. The fuel cell electric vehicles (FCEVs) using polymer electrolyte membrane fuel cells (PEMFCs) has many advantages over the internal combustion engine and other renewable energy vehicles such as high efficiency, zero emission, fast fueling, unique power and energy scalability (without heavy penalty from the increased mass)[1-3]. After two decades of intensive development, there are only several thousand FCEVs on the road, in contrast to the millions of battery electric vehicles (BEV) in use today[4, 5]. Beside the lack of hydrogen infrastructure, the major obstacle for the FCEV development is still the cost of the PEMFC system, in which the platinum group metal (PGM) catalysts count for up to 42% total cost of the PEMFC system, which becomes higher as the production scales up[6]. Although the current Pt usage has been reduced to 22.5 g Pt per 90 kW stack[7], the ultimate goal of 5 g Pt has still not been achieved[7, 8]. Further reduction of the Pt usage is critically needed for the PEMFC large-scale commercialization. Great effort has been devoted to the catalyst development for the oxygen reduction reaction (ORR) on both PGM and PGM-free material in the past decades[9-11]. However, the catalysts with excellent intrinsic catalytic performance measured by rotating disk electrode (RDE) do not always show promising performance in the membrane electrode assembly (MEA) which is the core component in PEMFC system. For instance, the Pt/Vulcan-XC72 (Pt/V) catalyst shows very high mass activity, 0.3 A/cm^2 at 0.90 V (vs. S.H.E) while in a MEA, such catalyst only shows around 0.15 A/cm^2 [12-14]. Also, Lazaridis et.al raised a discussion that the limited transferability of performance from RDE to MEA poses a major obstacle towards the rapid integration of promising electrocatalyst designs into actual PEM systems.[15]Hence, there has been a longstanding challenge for PEMFCs: how to translate the excellent intrinsic RDE performance of a catalyst into MEA.

The fundamental of this challenge lies on the structure of the catalyst layers (CLs) in RDE versus MEA. Within the RDE CL, each individual catalyst particle (i.e., Pt nanoparticle dispersed over the surface of carbon support) is well dispersed over the surface of a RDE glassy carbon disk and these catalyst particles are fully exposed to the liquid electrolyte (Figure 1a). Namely, the surface of each catalyst particle is almost 100% accessible for the electrolyte except the portion in contact with glassy carbon disc or with other particles[16]. Hence, a complete electrolyte/catalyst interface is established. Consequently, the dissolved oxygen molecules and the protons (H^+) can diffuse

from the bulk of the electrolyte to this interface to participate in the ORR while the electrons are transferred to the interface via the glassy carbon. With such a structure, every catalyst particle (except those agglomerated) is utilized for catalyzing ORR, achieving a very high catalyst utilization[16]. In contrast, in the CL of a MEA, instead of the liquid electrolyte, the ionomer is used to serve as the solid electrolyte (Figure 1b). Thus, an electrolyte (ionomer)/catalyst interface is formed, in which an ionomer film covers the surface of the catalyst nanoparticle (Figure 1c), and the ORR occurs at this interface. Note, unlike in the RDE CL, in which all exposed catalyst surface can form the electrolyte/catalyst interface, in a MEA CL, the exposed catalyst surface may not form the ionomer/catalyst interface if the surface is not covered by an ionomer film (Figure 1b). As the consequence, the benchmark testing showed that the tested catalyst performances are critically different in RDE and MEA. To be more specific, the performance difference is constrained by mass transfer and PGM utilization, which are results of the ionomer/catalyst interface in the MEA, as compared to the RDE.[17] Therefore, the performance difference between the RDE and MEA flows down to the difference on the interfaces. The transferability challenge can be transformed into the ultimate challenge of the fundamentals: how to build a perfect ionomer/catalyst interface (i.e., regarding the RDE interface, every catalyst particle is utilized) in a MEA CL. At this ionomer/catalyst interface, three species, O_2 molecules (diffusing through the ionomer film after long path from the pores of CL), proton H^+ (transferring along the ionomer film) and the electrons (flowing via carbon support first, then Pt particles) simultaneously reach the same site of the interface to complete the ORR (Figure 1c). Thus, the ionomer/catalyst interface becomes the centerpiece of the PEMFC from the fundamental perspective since this is where the ORR occurs.

For decades, the great effort has been dedicated to the CL/MEA development while little attention is paid to construct an ideal ionomer/catalyst interface with few exceptions: introducing the ionomer as both proton conductor and binder to replace the polytetrafluoroethylene (PTFE) binder, which revolutionized the CL/MEA structure[18, 19], but not purposely focused on the interface. In the current approaches, the catalyst powder and ionomer solution are mixed to form a catalyst ink. Then, such a catalyst ink is evaporated to remove the solvent and finally form a porous CL (Figure S1a). The formed ionomer/catalyst interface is the result of randomly precipitated ionomer agglomerate/film over the catalyst and carbon support surface, which is neither uniform nor thin due to oxygen containing groups (ketone, quinone, carboxylic, etc.) over the carbon surface[20 21],

which repels the ionomer particles due to the negative charged SO_3^- groups of the ionomer surface. Very often, this leads to a quite large catalyst surface being uncovered. To improve the interface, one approach is to use excessive amount of ionomer, which may increase the coverage but with the heavy penalty of increased O_2 diffusion barrier from crossing thicker ionomer film, reducing the high current density performance. Although a recent developed highly oxygen-permeable ionomer (HOIPs) can significantly improve the O_2 diffusion[19, 22] via ionomer film, the ionomer/catalyst interface remains a huge challenge. On the other hand, some researchers focus on optimal ionomer film on catalyst surface, for example, recently, Ott et al.[23] report a method of improving the ionomer distribution, which used Nitrogen (N) doped carbon, but the science behind this phenomenon is not discussed in detail, and the performance of catalyst supported on the N doped carbon is not significantly higher than catalyst supported by untreated carbon.

Here, we propose a novel approach to rationally design an ideal ionomer/catalyst interface and construct such an interface utilizing the electrostatic attraction force. Instead of uncontrolled thus random formation of ionomer/catalyst interface, we control the formation of the ionomer/catalyst interface in the liquid phase (i.e., catalyst ink) via charge attraction and an ionomer/catalyst interface is spontaneously formed with the more uniform and thin ionomer film (Figure 1d). Such a designed interface leads to excellent MEA performance in terms of mass activity, ECSA, and rated/peak power density, which is beyond the state-of-art (Table S3). In addition, this approach can be directly used to fabricate the high-performance MEA for PEMFCs, which will certainly accelerate the massive commercialization. Finally, this approach demonstrates a method of solving the practical engineering challenge with the solid and fundamental understanding on the issue through establishing property (ink)-structure (interface)-performance relationship.

RESULTS AND DISCUSSION

Design and Construction of the Ionomer/Catalyst Interface

The ideal ionomer/catalyst interface should have the following features: (1) the surface of the catalyst (except the portion in contact with carbon) should be completely covered by the ionomer film so that all Pt surface participates in the ORR, which, in turn, will lead to the almost 100% Pt utilization, so does the high mass activity and the electrochemical active surface area (ECSA), (2) the ionomer film should be as thin as possible to minimize the O_2 diffusion resistance through it so that the limiting current density can reach the maximum, consequently, the max power

performance. Meanwhile, the reduction of ionomer film thickness should not comprise the proton conduction. To utilize the charge attraction to control the formation of the interface, the surface of the carbon particles was covalently grafted with *p*-benzylamine group ($-NH_3^+$ after hydration) and then the Pt nanoparticles were loaded (assigned as Pt/V_{NH2}). When such a catalyst, Pt/V_{NH2}, with positive charge, $-NH_3^+$, is mixed with the ionomer particles in a water-based solution, similar to a self-assembly process, the negatively charged $-SO_3^-$ groups from the ionomer particles attract the positively charged catalyst Pt/V_{NH2} particles and the ionomer/catalyst interface is spontaneously formed in the liquid (Figure 1d). To prove this hypothesis, we used both positively charged catalyst, $Pt/V\text{-}NH_2$, and negatively charged catalyst Pt/V_{SO3H} to see if a promising interface or a poor interface is constructed, respectively. The negatively charged catalyst was synthesized using *p*-benzenesulfonic acid group ($-SO_3H$) functionalized carbon to load Pt nanoparticles following our previous work[21, 24]. Combining the XPS data in Figure S3 and the same results that showed in our previous publication[25], the surface functionalization is successfully realized. Additionally, an untreated catalyst Pt/Vulcan-XC72 labelled as Pt/V was used as the baseline. For all of catalysts, the Pt nanoparticle was controlled around 3.5 ± 0.5 nm with tight distribution (Figure S2d) to minimize effect of the particle size on MEA performance (The effect of such small range of particle size is negligible[25-27]). Moreover, the mass activity test of three catalysts from RDE shows that the intrinsic mass activity of these catalysts is similar (Figure S6). Further, the Vulcan XC72 was chosen as the catalyst support, which is low structure carbon with very few intraparticle pores, to exclude the accessibility issue of Pt nanoparticles trapped within the pores of high structure carbons (e.g., Ketjen Blacks EC300J or EC600)[28, 29]. Thus, the measured MEA performance must solely rely on the interface. These catalysts were systematically studied from the catalyst ink dispersion, interface, and the MEA performance using ultra small angle scattering x-ray (USAXS), cryo-TEM, isothermal-titration-calorimetry (ITC), HRTEM, 3-D FIB-SEM, mercury intrusion porosimetry (MIP), XPS, RDE and fuel cell testing to demonstrate the designed interface and reveal the property (ink)-structure (interface)-performance (MEA) relationship.

The Formation of the Designed Catalyst/Ionomer Interface in a Catalyst Ink

The dispersion of a catalyst powder (i.e., Pt nanoparticles supported on the surface of carbon particle) and an ionomer in solvents is the first step of fabricating a CL/MEA. In this step, the ionomer/catalyst interface is formed because both catalyst and ionomer particles can freely move

and interact in the solvent. Forming the interface relies on the electrostatic attraction, and it is critical to know if such an attraction exists between the positively charged Pt/V_{-NH2} catalyst and negatively charged ionomer particles in the dispersion. To determine the interaction between ionomer and three types of carbons, respectively, the binding entropy of these three pairs was measured using the method developed in our recent work of using ITC analysis to quantify the ionomer-catalyst interaction[30, 31]. Ionomer was titrated into the ink, and the heats of adsorption were measured then calculated to generate a binding isotherm. By fitting the isotherm to an independent (Langmuir) binding model, the association constant K_A for ionomer binding to nanoparticle can be extracted (Figure 1e). For ionomer binding to NH_2-XC72, K_A is greater than that for binding to XC72 on a mass basis, indicating a stronger interaction between ionomer and NH_2-XC72. Furthermore, the binding to SO_3H-XC72 was not detectable, indicating a weak or no attractive interaction between ionomer and SO_3H-XC72. Enthalpy is also extracted from the isotherm. The surface area-normalized enthalpic contributions for binding to NH_2-XC72 and XC72 (93.6 m^2/g, 254 m^2/g for NH_2-XC72 and blank-XC72, respectively) follow the same trend with K_A, see Figure 1f. Additional thermodynamic binding information can be extracted after making key assumptions (see SI for details Figure S4) to calculate the molar concentration of ionomer and catalyst binding sites for NH_2-XC72 and XC72, the entropic (Figure 1g) contribution is greater than the enthalpic contribution, consistent with previous observations for other ionomers[30, 31]. The entropic contribution, which is greater for NH_2-XC72, is attributed to liberated water molecules due to hydrophobic/hydrophilic interactions upon binding[32]. The surface area-normalized enthalpic contributions for binding to NH_2-XC72 and XC72 follow the same trend with K_A (Figures 1e&2bf). Based on these results, the positively charged -NH_3^+ functional group of catalyst particles strongly attracts the negatively charged –SO_3^- groups of ionomer particles once they meet. These ITC results match very well with our previous results from Zeta potential measurement[33]. The USAXS analysis[33, 34] of the same three dispersions indicates that average aggregate size of Pt/V-NH_2 and ionomer is the largest, and Pt/V in between, while Pt/V_{SO3H} is the smallest (Figure 2a). Besides, for Pt/V_{NH2}, aggregates size increases from 105.6 ± 3.5 nm to 146.0 ± 3.3 nm after mixing with ionomer in catalyst ink while the average particle size of Pt/V_{SO3H} decreased from 93.8 ± 2.8 nm to 91.4 ± 2.4 nm, showing basically no particle size change; the Pt/V, the average particle size increased from the 106 ± 1.8 nm to 116.0 ± 2.1 nm, comparing to that of Pt/V_{NH2} catalyst, the increment is relatively small, Figures 2b-2d. The increased average

aggregate size is the results of the ionomer particles surrounding the Pt/V_{NH2} particles, strongly suggesting that a strong ionomer/catalyst interaction occurs for NH_2-XC72 while the unchanged average aggregate size is the result of non-interaction for SO_3H-XC72, and the weak interaction strength with the blank XC72 is in between them. The cryo-TEM images of the dispersion confirmed the formation of the interface. In the cryo-TEM image of Pt/V_{NH2} catalyst ink (Figure 2e), the catalyst particle (the yellow circled regions) is surrounded by the ionomer (the red circled regions), which is the result of the interaction between positively charged $-NH_3^+$ on Pt/V_{NH2} catalyst particles and the negatively charged $-SO_3^-$ ionomer particles. Furthermore, the ionomer particles (red circle regions) can be seen spreading over around the catalyst particles (yellow circles), clearly demonstrating that there is an attractive electrostatic force which not only pulls the catalyst and ionomer particles together but also change the shape/geometry of the ionomer particles, overspreading and wrapping around the catalyst particles. On the other hand, it is totally opposite for SO_3H functionalized catalyst Pt/V_{SO3H} (Figure 2g). The ionomer and catalyst particles stay away from each other (yellow circled and red circled regions), which is the result of the repulsive electrostatic force pushing the catalyst particles away from ionomer particles. The ionomer particles are in a spherical shape, which is in consistent with the reversed micelle structure[35, 36] as we observed in our previous work[34]. For the pristine Pt/V catalyst (Figure 2f), there is a very weak interaction than that of Pt/V_{NH2} (Figure 2e). These interactions of ionomer and the different charged groups (i.e. positive, negative charged and base line XC72) catalysts show the similar trend as we previously studied for the three different carbon supports (i.e., NH_2-XC72 >XC-72>SO_3H-XC72) using both USAXS and cryo-TEM[33]. Note that the charges are over the carbon surface and the ionomer particles are attracted to the entire carbon surface while the Pt nanoparticle are also covered by the ionomer particles as the Pt nanoparticles are uniformly distributed over the carbon surface, hence, an ionomer/catalyst interface is formed. Overall, all results from ITC, USAXS and cryo-TEM clearly demonstrate the formation of the ionomer/catalyst interface in the catalyst ink for Pt/NH_2-XC72 catalyst.

The Ionomer/Catalyst Interface in Catalyst Layers

Cryo-TEM was employed to visualize distribution of thin ionomer layers over the carbon-supported Pt in the formed CL (after ink spraying and drying). TEM has been used to resolve ionomer layers on highly graphitic and non-carbon supports[37, 38], but it is more challenging to

distinguish ionomer from carbon on less graphitized supports like Vulcan. This is illustrated in a cryo-TEM image of the ionomer-free XC-72 powder shown in Figure S5a, where thin carbon indicated by arrows pointed layers could be easily misidentified as ionomer. Mapping the fluorine signal using spectroscopic methods such as electron energy loss spectroscopy (EELS) or energy dispersive X-ray spectroscopy (EDS) is another approach for distinguish ionomer from the carbon support, but the high sensitivity of the polymer to the electron beam typically limits the application of spectroscopy methods to thicker layers or agglomerates, even when cryogenic cooling is applied to slow radiolysis.[39, 40] The TEM image acquisition and analysis were performed as a double blind experiment to prevent any human bias during the recording or interpretation of the low dose cryo-EM data. The regions used for imaging were randomly selected by the instrument operator. Four researchers participated in image interpretation and analysis with no prior knowledge regarding the differences between the samples to determine if there was consensus regarding differences in ionomer distribution as a result of the surface treatment. Characteristic images from the Pt/V_{NH2}, Pt/V, and Pt/V_{SO3H} powders scraped from the cathode CL are shown in Figures 3a-3f. Thin films attributed to ionomer were more prevalent over the Pt/V_{NH2} particles (Figures 3a & 3c, red dash line circled regions) with respect to the Pt/V, in which bare carbon and Pt surfaces were intermittently interrupted by larger agglomerates (Figures 3c-3d red dash line circled regions). The thickest agglomerate in Figure 3f was observed (Figure 3e-3f) and confirmed to be ionomer by STEM-EELS (Figure S5d), although the F fluorine edge was fainter than expected, indicating that radiolysis damage occurs even under low dose cryo-TEM imaging conditions. The qualitative differences in ionomer dispersion observed in cryo-TEM image provides additional support to the theory that ionomer dispersion can be influenced by controlling the electrostatic charge of the carbon surface, as conceptualized in (Figure 1d).

It can be observed that the CLs of the three catalysts are significantly different. Each layer exhibited a different thickness, the NH_2 CL (Figure 4a) is the thickest (7.0 μm), Blank CL thickness is (4.4 μm) (Figure 4b), which between the NH_2 CL and the SO_3H CL which is the thinnest (1.5 μm), (Figure 4c). Since the catalyst loading and ionomer carbon (I/C) ratios are all same among them, namely, the differences in thickness are attributed to changes in the pore structure. To better understand the pore structure, the samples were subjected to the FIB/slice and view procedure, where sections of around 10 nm were sliced by FIB and then observed by SEM. Two of these

sections can be observed in Figures 4d and g (the movies of the entire slice and view process are shown in movies S1 and S2), which shows that the pore size distribution in NH_2 CL is significantly larger than in SO_3H CL. This is even more evident after visualizing the CLs after a 3-D reconstruction of all the slices taken (Figures.4e, h) (movies S3, S4). In addition, the mercury intrusion porosimetary (MIP) measurements give both the global view and local detailed information of the pore structures of catalyst CLs of these three catalysts (Figure 4f, i). The results match the thickness of these CLs, the largest pore volume in the range from 10 nm to 1000 nm is 0.666 mL g^{-1} in NH_2 CL, then 0.577 mL g^{-1} in the blank CL, and the lowest pore volume yielded from SO_3H CL, 0.258 mL g^{-1}. The pore structure in this range strongly affects the O_2 mass transport in gas phase within a CL. For more details, the 3-D structure of pore is shown in Figurs.4e, h and Movies S3, S4, in which pores were presented by yellow color. It is clear that there is huge difference of pores size distribution and total pore volume between the NH_2 and SO_3H CLs. For such a pore structure of NH_2 CL, one hypothesis is that the formed large Pt/V_{NH2} and ionomer particles (measured by USAXS) resulting from the interaction leads to low packing ratio, causing increasing the pore volume. Another possibility is that the shrinkage of the ionomer film surrounding the Pt/V_{NH2} in a CL leads to more void space.

The Electrochemical Characterization (RDE/MEA)

The intrinsic catalytic performance of these three catalysts was determined using RDE. In order to eliminate the effect of the different interactions between catalyst and ionomer, ionomer free catalyst inks were used for RDE testing [41]. Mass activities (MA) of these three catalysts from RDE are quite close: 298 $mA \cdot mg^{-1}_{Pt}$, 286 $mA \cdot mg^{-1}_{Pt}$, and 278 $mA \cdot mg^{-1}_{Pt}$ for Pt/V_{NH2}, Pt/V and Pt/V_{SO3H}, respectively (Figure S6). The almost identical polarization curves of these three catalysts also suggest that they have very similar intrinsic ORR performance.

For all three catalysts, the positively charged Pt/V_{NH2} catalyst MEA shows the highest performance (Figure 5a), ECSA, and mass activity (Figure 5b) while the negatively charged Pt/V_{SO3H} MEA has the lowest mass activity and ECSA. Not surprisingly, the Pt/V MEA is in the middle. The measured mass activity in MEA is 190 mA cm^{-2}, 160 mA cm^{-2}, and 78 mA cm^{-2} and ECSA is 52.38 $m^2\ g^{-1}_{Pt}$, 46.42 $m^2\ g^{-1}_{Pt}$, and 25.31 $m^2\ g^{-1}_{Pt}$ for Pt/V_{NH2}, Pt/V, and Pt/V_{SO3H}, respectively (Figure 5b). This demonstrated that the ionomer coverage over Pt nanoparticles is different for three catalysts: the ionomer coverage is the highest for Pt/V_{NH2} and the lowest for Pt/V_{SO3H}. Consequently, this higher

ionomer coverage leads to higher Pt utilization, and higher mass activity, which indicates that there is a higher ionomer/catalyst interface for Pt/V_{NH2} than Pt/V_{SO3H}. This highest mass activity and ECSA of Pt/V_{NH2} proves that our hypothesis of constructing the ionomer/catalyst interface utilizing the charge attraction does work as we designed. The Pt/V_{NH2} MEA achieved the outstanding performance among these three catalysts not only in kinetic controlled region (i.e., mass activity and ECSA), but also in mixing controlled and mass transfer-controlled regions (i.e., rated/peak power density). The rated power density (power density at 0.67 V) of Pt/V_{NH2} MEA reached 910 mW cm^{-2} which is not only outstanding above other two catalysts, but is also comparable with published high active Pt alloy catalyst like PtNi[42], PtNiN[12], and PtCo[43], see more detail in Supplementary Table II. The rated power density of Pt/V and Pt/V_{SO3H} catalyst MEAs are 729 mW cm^{-2} and 440 mW cm^{-2}, respectively (Figures 5c, d). Further, the helox (21 vol% O_2 in He) test was performed on three MEAs following the H_2/air test on same MEA to unravel the O_2 diffusion resistance in N_2. The performance gains of MEA from testing in helox against in air represents the O_2 transfer resistance in gas phase, i.e., in N2 blanket[44]. In Figure S8, performance gains of three MEAs follows the trend that NH_2<Blank<SO_3H. Less performance gain suggests high porosity in CL, and it is consistent with the MIP and FIB-SEM result forementioned.

The highest rated power density from Pt/V_{NH2} MEA is the evidence that the formed ionomer film over the Pt nanoparticles is more uniform and thinner than those of Pt/V and Pt/V_{SO3H} catalyst MEAs. In high current density region, the diffusion of O_2 molecule through the ionomer film of the interface to reach the Pt surface is the rate-limiting step with the assumption that the O_2 molecule diffusion in the N_2 blanket (i.e., air) through the pores of the CL is much faster. Hence, the current density of a CL of a MEA is controlled by the liming current density of O_2 molecule diffusing through the ionomer film. The thinner the ionomer film is, the shorter the O_2 molecule diffusion length in the ionomer film is, and the higher the limiting current density is. Since all MEAs of these three catalysts used the same I/C ratio, namely, the same ionomer content, then, the uniform distributed ionomer over catalyst and carbon support surface (same particle size, same surface area) of Pt/V_{NH2} should have thinner ionomer film than the non-uniformed one, Pt/V_{SO3H}.

O_2 Diffusion in Ionomer Film of the Interface

To further prove that the O_2 molecule diffusion via ionomer film (i.e., O_2 transport resistance) is the limiting step and the Pt/V_{NH2} has the more uniform and thinner ionomer film than that of

Pt/V_{SO3H}, the O_2 molecule diffusion resistance (R_{total}, (s/m))was studied. R_{total} is defined as the total diffusion resistance from the outer surface of the diffusion media to the surface of the Pt nanoparticle, where R_{DM} is the O_2 diffusion resistance in diffusion media. The O_2 of the air transport within a CL consists of two processes: O_2 molecules diffuse in the N_2 blanket (i.e., air) within the pores of the CL to reach the ionomer/catalyst interface, and then O_2 molecules diffuse through the ionomer film to reach the surface of Pt nanoparticles (Figure 1c). The effect of mass transport usually is expressed as the transport resistance. The resistance of O_2 transport in N_2 gas is named gas phase transport resistance ($R_{CL,gas}$, (s/m)) and mainly controlled by pore structure of CL, and the diffusion resistance through ionomer film to catalyst surface named solid phase transport resistance ($R_{CL,ion}$, (s/m)).

$$R_{total} = R_{DM} + R_{CL,gas} + R_{CL,ion} \quad \text{(Eq.1)}$$

To quantify how much improvement that NH_2 caused by enlarging ionomer coverage and consequently, reducing the thickness of ionomer film on the catalyst carbon support (CCS), limiting current density measurements were conducted at different relative humidity for all three catalysts. To begin with, q is defined as an index to reflect the quality of ionomer film over CCS, and $q = \frac{\delta_{ion}^{eff}}{A_{ion}^{eff}}$. Where δ_{ion}^{eff} is the effective ionomer thickness (m) and A_{ion}^{eff} is the effective ionomer area for oxygen permeation ($m^2 \cdot m^{-2}$). The large q value indicates either the large δ_{ion}^{eff} (suggesting thicker ionomer film) or the small A_{ion}^{eff} (suggesting small efficient ionomer coverage), which results in either slow diffusion of O_2 molecule through the ionomer film on CCS (poorer high current density performance) or lower catalyst utilization (lower MA and ECSA). Vice versa, smaller q value suggests that either the small δ_{ion}^{eff} (suggesting thinner ionomer film) or the large A_{ion}^{eff} (suggesting larger efficient ionomer coverage), which results in either faster diffusion of O_2 molecules through the ionomer film on CCS (much improved high current density performance) or higher catalyst utilization (higher MA and ECSA).

The relationship between q *and* $R_{CL,ion}$ was established in Eq.2 based on the modeling work of Nobuaki Nonoyama and coworkers[45]. $R_{CL,ion}$ is related to q and $\Psi_{ion,O2}$, the oxygen permeability coefficient, $(mol \cdot s^{-1} \cdot m^{-1} \cdot Pa^{-1})$ and $\Psi_{ion,O2,}$ is defined in Eq.3.

$$R_{CL,ion} = \frac{q}{\Psi_{ion,O_2} RT} \quad \text{(Eq.2)}$$

$$\Psi_{ion,O_2} = \frac{D_{ion,O_2}}{H_{ion,O_2}} = 3.27 \times 10^{-15} \exp\left[1.28(RH)\right] \times \exp\left[\frac{17{,}200}{R}\left(\frac{1}{323.15} - \frac{1}{T}\right)\right] \quad \text{(Eq.3)}$$

Where D_{ion,O_2} is the diffusivity of O_2 in ionomer ($m^2 \cdot s^{-1}$) and H_{ion,O_2} is the Henry constant of O_2 ($Pa \cdot m^3 \cdot mol^{-1}$). At a given temperature, $\Psi_{\text{ion,O2}}$, $(mol \cdot s^{-1} \cdot m^{-1} \cdot Pa^{-1})$, is only the function of relative humidity (RH) (see SI for details). For a given MEA at a fixed temperature, q is a constant (i.e. MEA structure is fixed) and thus $R_{CL,ion}$ is determined by $\Psi_{\text{ion,O2}}$. It is important to point out that $\Psi_{\text{ion,O2}}$ is the property of both oxygen and ionomer. Then, a relationship of q and R_{total} was established in Eq.4 (See SI for detailed derivation):

$$q = \left(R_{total}^{RH_1} - R_{total}^{RH_2}\right) b \quad \text{(Eq.4)}$$

where b is constant at given temperature (i.e., 80 °C). $R_{total}^{RH_1}$ and $R_{total}^{RH_2}$ are R_{total} at RH_1 and RH_2, respectively. For a given MEA, the $R_{CL,gas}$ and R_{DM} remain constant because R_{DM} , $R_{CL,gas}$ (i.e., pore structure of CL) do not change with RHs. We measured ionic conductivity of CL using the method from our previous work for three types of catalyst[46]. We find the ionic conductivity of three types of CL does not have very significant change under different RHs (i.e., 50% and 80% RH), see Figure S9. Overall, since the R_{total} is the sum of R_{DM}, $R_{CL,ion}$, and $R_{CL,gas}$ (Eq.1), the difference of R_{total} at two different RHs: RH_1 and RH_2, $\Delta R_{total} = R_{total}^{RH_1} - R_{total}^{RH_2}$ should be equal to the difference of $R_{CL,ion}$ at two different RHs: $\Delta R_{CL.ion} = R_{CL.ion}^{RH_1} - R_{CL.ion}^{RH_2}$.

There is a sophisticated method to calculate the R_{total} in cathode: limiting current density analysis [45]. R_{total} can be obtained from the intercept of the linear plotting of total O_2 mass transfer resistance in MEA hardware against back pressure[47, 48] (Figures 6a-c). Limiting current density measurements were conducted at different RHs (i.e., 50% and 80% RH) to obtain the R_{total}. Measurement at 100 % RH was avoided to exclude the possible interference of liquid water on O_2 transfer[49], especially the SO_3H catalyst (Figure S10c). The results show that $R_{total,80\,\%RH}$ is the smallest in all R_{total}s (Figure 6d), hence, $R_{total,80\,\%RH}$ was chosen as the reference to ensure all ΔR_{total} are positive value. The difference of R_{total} between two RHs is assigned as $\Delta R_{total,\,80,20}$. Not surprisingly, $\Delta R_{total,80,20}$ of the MEA of Pt/V_{NH2} is 2.48E-2 s m^{-1}, the smallest among three MEAs while the largest difference, 15.1E-2 was seen for the MEA of Pt/V_{SO3H}, and the blank MEA of Pt/V is 5.57E-2 s m^{-1}. These values are related to q of each CL, consequently, reflecting their

ionomer/catalyst interface. The smallest $\Delta R_{total,80,20}$ indicates that the best interface is the Pt/V_{NH2} while the largest $\Delta R_{total,80,20}$ suggests that the worst interface is the Pt/V_{SO3H}.[47, 48] (Figure 6d).

To compare the thickness of ionomer films in the ionomer/catalyst interfaces of three MEAs, further limiting current analysis was carried out. Two MEA q_{Blank} and q_{NH_2} are related in the following equation,

$$\frac{q_{Blank}}{q_{NH_2}} \approx \frac{\delta_{ion\,Blank}^{eff}\, A_{PtNH_2}}{\delta_{ion\,NH_2}^{eff}\, A_{PtBlank}} \approx \frac{\delta_{ion\,Blank}^{eff}\, ECSA_{NH_2}}{\delta_{ion\,NH_2}^{eff}\, ECSA_{Blank}} \quad \text{(Eq.5)}$$

Where A_{PtNH_2} and $A_{PtBlank}$ are surface areas of Pt nanoparticles in Pt/V_{-NH2} and Pt/V CLS respectively. Plug the ECSA values in Figure 3b, the Eq.5 becomes the Eq.6 below and plug the measured $\Delta R_{total} = R_{total}^{RH_1} - R_{total}^{RH_2}$ for the blank and NH_2 respectively, Eq.5 becomes Eq.7.

$$\frac{q_{Blank}}{q_{NH_2}} \approx \frac{\delta_{ion\,Blank}^{eff}\, ECSA_{NH_2}}{\delta_{ion\,NH_2}^{eff}\, ECSA_{Blank}} = \frac{\delta_{ion\,Blank}^{eff}}{\delta_{ion\,NH_2}^{eff}} \times 0.87 \quad \text{(Eq.6)}$$

$$\frac{q_{Blank}}{q_{NH_2}} = \frac{\left(R_{total}^{RH_1} - R_{total}^{RH_2}\right)_{Blank}}{\left(R_{total}^{RH_1} - R_{total}^{RH_2}\right)_{NH_2}} = \frac{0.05656}{0.02448} \quad \text{(Eq.7)}$$

Solve Eq.6 and Eq.7 simultaneously, we get the ratio of effective thickness of two ionomer films, blank vs. NH_2 as below,

$$\frac{\delta_{ion\,Blank}^{eff}}{\delta_{ion\,NH_2}^{eff}} \approx 2.66 \quad \text{(Eq.8)}$$

Similarly, we can get the ratio of two ionomer, SO_3H vs. NH_2 as below,

$$\frac{\delta_{ion\,SO_3H}^{eff}}{\delta_{ion\,NH_2}^{eff}} \approx 12.90 \quad \text{(Eq. 9)}$$

The $R_{CL,ion}$ is normalized by combining the resistance of O_2 diffusion through ionomer film ($R_{CL,\,ion-film}$) and the interfacial resistance of O_2 diffusion of ionomer and Pt NP ($R_{CL,\,ion\&Pt\,interface}$)[50, 51]. The average normalized thickness of ionomer film in the blank CL is

close to 3 times that in NH_2 CL. Moreover, the normalized ionomer film thickness in the SO_3H CL is almost thirteen times that in NH_2 CL.

MEA Stability

Furthermore, the stability of Pt/V_{NH2}, Pt/V, and Pt/V_{SO3H} catalysts were evaluated (Figure. S11) using the standard accelerating stress testing (AST) protocol recommended by the US Department of Energy (DOE), i.e., trapezoidal wave method from 0.6 V to 0.95 V with 0.5 s rise time and 2.5 s holding time (H_2/N_2, 80 °C, 100 % RH, 50/75 sccm). For example, after 30k AST cycles, the measured mass activity losses of the Pt/V_{NH2} and Pt/V_{SO3H} are around 36% which are lower than that of Pt/V, 42%, suggesting that using the functionalized carbon supports, the catalyst stability in high voltage range increases. This result agrees well with our previous result in RDE[52]. However, at 0.8 A cm^{-2}, the voltage loss of Pt/V_{SO3H} is 138 mV, which is more than double of those of Pt/V_{NH2} and Pt/V, i.e., 54 mV and 50 mV, respectively (Supplementary Table IV). The possible reason is that the poor ionomer network resulting from the unevenly distributed ionomer film over the Pt/V_{SO3H} catalyst is easier to be damaged so that the ionomer network fails drastically, resulting in the serious issue of proton transfer. On the other hand, the stability of Pt/V_{NH2} is similar with that of Pt/V, suggesting using NH_2 functionalized carbon support, the performance is improved without compromising the stability in the low voltage range. The stability of a catalyst after surface modification is an interesting topic, but a clear understanding of this requires much operando experiment to observe the degradation of the grafted groups and most importantly, the ionomer network, which are beyond the scope of this work. However, we plan to explore this topic further and share our results in future work.

CONCLUSIONS

Realizing that the critical issues for PEMFC performance lie on the ionomer/catalyst interface in a CL/MEA where the ORR occurs, the essential and fundamental challenge for the ultimate PEMFC performance is to build an ideal ionomer/catalyst interface which has the maximum ionomer coverage for Pt utilization and as thin as possible ionomer film for oxygen diffusion. The ideal ionomer/catalyst interface has been proposed, designed, and realized utilizing the surface charge attraction between the positively charged catalyst particles and negatively charged ionomer: the chemically grafted groups such as the NH_2, which carries positive charge in an aqueous solution has strong interaction with the negatively charged SO_3H in ionomer particles. The strong

charge attraction changes the shape/geometry of the ionomer particles and makes them surround the positively charged catalyst particles to form a more uniform and much thinner ionomer film over than the conventional approach. The formation of such an ideal interface is spontaneous process (which is similar to the self-assembly process) and is controllable by adjusting the surface charge density. Such an interface effectively promotes the Pt utilization and the O_2 diffusion through ionomer film. Additionally, such an interface leads to a highly porous structure in the catalyst layer, which strongly boosts the O_2 transfer, consequently, the high current density performance without compromising the O_2 transfer through it. The comprehensive characterization of three cases of positively charged, negatively charged and the pristine catalysts proves the formation of such ionomer/catalyst interface in a catalyst ink for positively charged catalyst (rather through evaporation process), which is preserved into a solid catalyst layer with the consequent superior MEA performance. The modeling and the limiting current measurement further prove the formation of the ideal interface in a catalyst layer with much higher ionomer coverage and thinner ionomer film over catalyst particles. All of the work demonstrates that our design of ideal ionomer/catalyst interface and the realization of such interface are essential for the ultimate PEMFC performance. Such a concept of the ideal interface is paramount of importance to all reactions involving the solid/gas/liquid interface such as heterogonous catalysis (i.e., water electrolysis and electrolysis in alkali industry, etc.) and other applications (i.e., solid-state batteries, etc.). This opens a new avenue for developing highly efficient devices for energy conversion/storage (i.e., fuel cells, batteries), hydrogen production (i.e., water electrolysis) and other applications (i.e., alkaline industry). This work also suggested that with thorough understanding of the challenges, solving the problem from the fundamentals, the interface of ionomer/catalyst, and designing the ideal interface and engineering to construct such interface based on the relationship of the property-structure-performance, is an innovative approach for dealing with complicated challenges we are facing today.

ACKNOWLEDGEMENT

The authors would like to thank Dr. Sarah A. Berlinger and Dr. Behzad Rad for helpful discussions. This work is supported by the Million Mile Fuel Cell Truck (M2FCT) Consortium (https://millionmilefuelcelltruck.org), technology manager Greg Kleen, which is supported by the U.S. Department of Energy, Office of Energy Efficiency and Renewable Energy, Hydrogen and Fuel Cell Technologies Office, under contract number DE-AC02-05CH1123. ITC work at the

Molecular Foundry was supported by the Office of Science, Office of Basic Energy Sciences, of the U.S. Department of Energy under Contract No. DE-AC02-05CH11231. A.B. acknowledges support from the Graduate Research Fellowship Program by the National Science Foundation under Grant No. DGE 1752814. This research used resources of the Advanced Photon Source; a U.S. Department of Energy (DOE) Office of Science User Facility operated for the DOE Office of Science by Argonne National Laboratory under Contract No. DE-AC02-06CH11357. High-resolution cryo-TEM was conducted at the Center for Nanophase Materials Sciences, which is a DOE Office of Science User Facility. The authors acknowledge the support by FCT, through IDMEC, under LAETA, project UIDB/50022/2020.

REFERENCES

1. D. A. Cullen, K. C. Neyerlin, R. K. Ahluwalia, R. Mukundan, K. L. More, R. L. Borup, A. Z. Weber, D. J. Myers and A. Kusoglu, *Nature Energy*, 2021, **6**, 462-474.
2. H. A. Gasteiger and N. M. Markovic, *Science*, 2009, **324**, 48-49.
3. F. T. Wagner, B. Lakshmanan and M. F. Mathias, *The Journal of Physical Chemistry Letters*, 2010, **1**, 2204-2219.
4. G. Bauer, C.-W. Hsu, M. Nicholas and N. Lutsey, 2021.
5. Y. L. Ding, Z. P. Cano, A. P. Yu, J. Lu and Z. W. Chen, *Electrochemical Energy Reviews*, 2019, **2**, 1-28.
6. J. T. Fan, M. Chen, Z. L. Zhao, Z. Zhang, S. Y. Ye, S. Y. Xu, H. J. Wang and H. Li, *Nature Energy*, 2021, **6**, 475-486.
7. A. Kongkanand and M. F. Mathias, *J Phys Chem Lett*, 2016, **7**, 1127-1137.
8. A. Ohma, T. Mashio, K. Sato, H. Iden, Y. Ono, K. Sakai, K. Akizuki, S. Takaichi and K. Shinohara, *Electrochimica Acta*, 2011, **56**, 10832-10841.
9. X. X. Wang, M. T. Swihart and G. Wu, *Nature Catalysis*, 2019, **2**, 578-589.
10. D. Banham and S. Ye, *ACS Energy Letters*, 2017, **2**, 629-638.
11. Y. Shao, J. P. Dodelet, G. Wu and P. Zelenay, *Adv Mater*, 2019, **31**, e1807615.
12. X. R. Zhao, C. Xi, R. Zhang, L. Song, C. Y. Wang, J. S. Spendelow, A. I. Frenkel, J. Yang, H. L. Xin and K. Sasaki, *Acs Catalysis*, 2020, **10**, 10637-10645.
13. Z. Qiao, C. Y. Wang, C. Z. Li, Y. C. Zeng, S. Hwang, B. Y. Li, S. Karakalos, J. Park, A. J. Kropf, E. C. Wegener, Q. Gong, H. Xu, G. F. Wang, D. J. Myers, J. Xie, J. S. Spendelow and G. Wu, *Energy & Environmental Science*, 2021, **14**, 4948-4960.
14. S. Kabir, D. J. Myers, N. Kariuki, J. Park, G. Wang, A. Baker, N. Macauley, R. Mukundan, K. L. More and K. C. Neyerlin, *ACS Appl Mater Interfaces*, 2019, **11**, 45016-45030.
15. T. Lazaridis, B. M. Stühmeier, H. A. Gasteiger and H. A. El-Sayed, *Nature Catalysis*, 2022, **5**, 363-373.
16. H. A. Gasteiger, S. S. Kocha, B. Sompalli and F. T. Wagner, *Appl Catal B-Environ*, 2005, **56**, 9-35.
17. R. Riasse, C. Lafforgue, F. Vandenberghe, F. Micoud, A. Morin, M. Arenz, J. Durst and M. Chatenet, *Journal of Power Sources*, 2023, **556**.
18. M. S. Wilson and S. Gottesfeld, *Journal of the Electrochemical Society*, 1992, **139**, L28-L30.
19. R. Jinnouchi, K. Kudo, K. Kodama, N. Kitano, T. Suzuki, S. Minami, K. Shinozaki, N. Hasegawa and A. Shinohara, *Nat Commun*, 2021, **12**, 4956.
20. K. Kinoshita, *Carbon: Electrochemical and Physicochemical Properties*, John Wiley & Sons, New York, 1988.
21. F. Xu, M. X. Wang, L. L. Sun, Q. Liu, H. F. Sun, E. A. Stach and J. Xie, *Electrochimica Acta*, 2013, **94**, 172-181.
22. J. Braaten, J. Liu, Z. White, N. Tiwari, G. Brown, A. M. Park, D. Paul, Z. Ulissi and S. Litster, *ECS Meeting Abstracts*, 2021, **MA2021-02**, 1188-1188.
23. S. Ott, A. Orfanidi, H. Schmies, B. Anke, H. N. Nong, J. Hubner, U. Gernert, M. Gliech, M. Lerch and P. Strasser, *Nat Mater*, 2020, **19**, 77-85.
24. L. Xin, F. Yang, J. Xie, Z. W. Yang, N. N. Kariuki, D. J. Myers, J. K. Peng, X. H. Wang, R. K. Ahluwalia, K. Yu, P. J. Ferreira, A. M. Bonastre, D. Fongalland and J. Sharman, *Journal of the Electrochemical Society*, 2017, **164**, F674-F684.
25. Z. Yang, S. Ball, D. Condit and M. Gummalla, *Journal of the Electrochemical Society*, 2011, **158**, B1439-B1445.
26. M. Shao, A. Peles and K. Shoemaker, *Nano Lett*, 2011, **11**, 3714-3719.
27. M. Gummalla, S. C. Ball, D. A. Condit, S. Rasouli, K. Yu, P. J. Ferreira, D. J. Myers and Z. W. Yang, *Catalysts*, 2015, **5**, 926-948.
28. I. Balberg, *Carbon*, 2002, **40**, 139-143.

29. J. H. Smuckler and P. M. Finnerty, in *Fillers and Reinforcements for Plastics*, AMERICAN CHEMICAL SOCIETY, 1974, vol. 134, ch. 17, pp. 171-183.
30. M. Thoma, W. Lin, E. Hoffmann, M. M. Sattes, D. Segets, C. Damm and W. Peukert, *Langmuir*, 2018, **34**, 12324-12334.
31. S. A. Berlinger, B. D. McCloskey and A. Z. Weber, *Acs Energy Letters*, 2021, **6**, 2275-2282.
32. S. A. Berlinger, B. D. McCloskey and A. Z. Weber, *J Phys Chem B*, 2018, **122**, 7790-7796.
33. F. Yang, L. Xin, A. Uzunoglu, Y. Qiu, L. Stanciu, J. Ilavsky, W. Li and J. Xie, *ACS Applied Materials & Interfaces*, 2017, **9**, 6530-6538.
34. F. Xu, H. Zhang, J. Ilavsky, L. Stanciu, D. Ho, M. J. Justice, H. I. Petrache and J. Xie, *Langmuir*, 2010, **26**, 19199-19208.
35. G. Gebel, *Polymer*, 2000, **41**, 5829-5838.
36. T. K. Bronich, A. M. Popov, A. Eisenberg, V. A. Kabanov and A. V. Kabanov, *Langmuir*, 2000, **16**, 481-489.
37. M. Barreiros Salvado, P. Schott, L. Guétaz, M. Gerard, T. David and Y. Bultel, *Journal of Power Sources*, 2021, **482**.
38. K. Kakinuma, R. Kobayashi, A. Iiyama and M. Uchida, *Journal of the Electrochemical Society*, 2018, **165**, J3083-J3089.
39. L. G. A. Melo, A. P. Hitchcock, J. Jankovic, J. Stumper, D. Susac and V. Berejnov, *ECS Transactions*, 2017, **80**, 275-282.
40. D. A. Cullen, R. Koestner, R. S. Kukreja, Z. Y. Liu, S. Minko, O. Trotsenko, A. Tokarev, L. Guetaz, H. M. Meyer, C. M. Parish and K. L. More, *Journal of the Electrochemical Society*, 2014, **161**, F1111-F1117.
41. A. Orfanidi, P. Madkikar, H. A. El-Sayed, G. S. Harzer, T. Kratky and H. A. Gasteiger, *Journal of The Electrochemical Society*, 2017, **164**, F418-F426.
42. B. H. Han, C. E. Carlton, A. Kongkanand, R. S. Kukreja, B. R. Theobald, L. Gan, R. O'Malley, P. Strasser, F. T. Wagner and Y. Shao-Horn, *Energy & Environmental Science*, 2015, **8**, 258-266.
43. J. Liang, N. Li, Z. Zhao, L. Ma, X. Wang, S. Li, X. Liu, T. Wang, Y. Du, G. Lu, J. Han, Y. Huang, D. Su and Q. Li, *Angew Chem Int Ed Engl*, 2019, **58**, 15471-15477.
44. H. A. Gasteiger, W. Gu, R. Makharia, M. F. Mathias and B. Sompalli, in *Handbook of Fuel Cells*, 2010, DOI: 10.1002/9780470974001.f303051.
45. N. Nonoyama, S. Okazaki, A. Z. Weber, Y. Ikogi and T. Yoshida, *Journal of the Electrochemical Society*, 2011, **158**, B416-B423.
46. C. Z. Li, Y. D. Liu, L. Xin, Y. K. Yu, Q. Gong, F. Yang and J. Xie, *Journal of the Electrochemical Society*, 2020, **167**.
47. D. R. Baker, D. A. Caulk, K. C. Neyerlin and M. W. Murphy, *Journal of The Electrochemical Society*, 2009, **156**.
48. K. C. Neyerlin, W. B. Gu, J. Jorne and H. A. Gasteiger, *Journal of the Electrochemical Society*, 2006, **153**, A1955-A1963.
49. A. Z. Weber, R. L. Borup, R. M. Darling, P. K. Das, T. J. Dursch, W. Gu, D. Harvey, A. Kusoglu, S. Litster, M. M. Mench, R. Mukundan, J. P. Owejan, J. G. Pharoah, M. Secanell and I. V. Zenyuk, *Journal of The Electrochemical Society*, 2014, **161**, F1254-F1299.
50. T. A. Greszler, D. Caulk and P. Sinha, *Journal of the Electrochemical Society*, 2012, **159**, F831-F840.
51. K. Kudo, T. Suzuki and Y. Morimoto, *ECS Transactions*, 2019, **33**, 1495-1502.
52. L. Xin, F. Yang, S. Rasouli, Y. Qiu, Z.-F. Li, A. Uzunoglu, C.-J. Sun, Y. Liu, P. Ferreira, W. Li, Y. Ren, L. A. Stanciu and J. Xie, *ACS Catalysis*, 2016, **6**, 2642-2653.
53. C. M. Popescu, C. A. S. Hill, R. Anthony, G. Ormondroyd and S. Curling, *Polymer Degradation and Stability*, 2015, **111**, 263-268.
54. D. Charriere and P. Behra, *J Colloid Interface Sci*, 2010, **344**, 460-467.

EXPERIMENTAL PROCEDURES

Catalyst functionalization and synthesis. The introduction of the NH_2 groups on carbon surface was realized using the diazonium reaction. *P*-phenylenediamine, Vulcan XC72 and nitric acid were mixed in a flask, sonicating using sonication bath, and then the mixture was heated to 65 ℃ in oil bath, and finally sodium nitrite solution was added into the mixture dropwise followed by 18 hrs-heating in an oil bath at 65 ℃. The same method was applied for SO_3H functionalization but replacing *P*-phenylenediamine with sulfanilic acid. After the reaction, the mixture was washed using DI-water and ethanol, then filtered, and dried in a vacuum oven over night at 60 ℃. The synthesized functionalized carbons were analyzed using XPS. The XPS results show the existence of NH_2 and SO_3H groups introduced on carbon surface with covalent bonded (FigS.2). After confirming the covalently bonded NH_2 and SO_3H groups onto carbon surface, then Pt nanoparticles were loaded by reducing precursor (H_2PtCl_2) in mixture of ethylene glycol and DI water at 140 °C for 6 hours. Finally, the dispersion was filtered followed by drying overnight in a vacuum oven at 60 °C over night.

USAXS measurement. The X-ray scattering measurements were conducted at beamline 9ID-C at the Advanced Photon Source (APS), Argonne National Laboratory. The samples of inks after sonication were collected into a glass capillary tube (5 mm diameter, NMR testing tube) and sealed with a rubber cap. The sample tubes were mounted in the beamline hutch and exposed to a 21 keV monochromatic X-ray beam. The scattered intensity was collected within a scattering vector range of 10^{-4} to 1 $Å^{-1}$ by using a Bonse-Hart camera setup for USAXS and a Pilatus 100 K detector for pinhole SAXS. The background scattering data from the capillary tube filled with the corresponding solvent (n-PA/H_2O) was recorded and subtracted from scattering data for each corresponding catalyst ink. The scattering data were analyzed in a modeling macro package Irena for data fitting and simulation on Igor Pro (WaveMetrics, OR) platform.

Cryo-TEM analysis. A 3.0 uL aliquot of the sample was placed on a glow discharged QUANTIFOIL® R1.2/1.3 300 mesh copper grid. It was then plunge-frozen using FEI Vitrobot Mark III with 8 sec blotting at 20 °C. The frozen grid was loaded into 200 kV Thermo Scientific Glacios™ Cryo Transmission Electron Microscope. Low dose images were recorded using Gatan K3 direct electron detector at ×45,000 nominal magnifications (0.88 Å/pixel) with total dose of 45 e/$Å^2$.

SEM Analysis of catalyst layer (MEA CL pore structure). MEAs of pristine-carbon black, NH_2-XC72 and SO_3H-XC72 samples were initially coated with a Gatan-J1 epoxy mixture to improve stiffness, placed in a mold filled with an Araldite® 6005, benzyl dimethylamine and docenyl succinic anhydride mixture, out-gassed to remove air at the MEA/epoxy interface, and cured in an oven at 60 °C for 8 hours. The cured molds were microtomed at room temperature and the electron transparent MEA cross-sections less than 70

nm thick were obtained for TEM observation. To acquire the pore morphology in the MEA CL of three catalysts, a focused ion beam (FIB) coupled with scanning electron microscope (SEM) was utilized in a slice and view mode (FigureS10). The thickness of each slice was controlled at 10nm, while the current of ion beam was controlled at 7.7pA to mitigate ion beam damage. In addition, the accelerating voltage of electron beam is controlled at 5kV for imaging, after each slicing by the ion beam. A global segmentation was first performed, followed by a manual segmentation and 3D reconstruction to achieve a more precise outline of pores in each image.

TEM analysis of ionomer/catalyst interface

The cathode was scrapped lightly with a razor and the resulting powder was ground and dispersed onto a lacey-carbon film supported on a 200 meshes copper grid. The grids were loaded into a Thermo Scientific Krios G4 cryo-TEM at room temperature, after which the instrument was cooled to cryogenic temperatures. Low-dose, high resolution images were acquired using a Thermo Scientific Falcon 4i direct electron detector with the accelerating voltage set to 300kV.

ITC Measurement

Binding experiments were conducted using a NanoITC (TA Instruments) as previously described[31]. Briefly, ionomer samples are dialyzed in deionized water and then diluted to 3.25 mg/mL for binding to SO_3H-XC72 and XC72 and diluted to 2.75 mg/mL for binding to NH_2-XC72 due to the stronger affinity. Ionomer is titrated into a cell containing 0.5 mg/mL nanoparticle in deionized water. For each experiment, an initial 4 uL ionomer aliquot is injected to remove bubbles; this injection is excluded from the data analysis. Twelve 8 uL aliquots of ionomer were injected into the cell at 25^{o}C, with 900 seconds between the start of each injection. Backgrounds were collected (water into nanoparticle, ionomer into water, and water into water) to subtract heats of dilution/mixing from the results. Each injection peak is then integrated, and the heats are fit to an independent binding isotherm using the NanoAnalyze software (TA Instruments). The association constant is extracted from the model fit, and error bars are obtained from the confidence interval of the fit.

Surface energy measurement

The surface energy of three carbons with water was measured using the dynamic vapor sorption (DVS) analysis (Micrometrics, Georgia, US). A sample was held at each temperature to reach the equilibrium while the mass change of the sample was measured at each temperature (RH). The mass change at each temperature (RH) step was recorded to generate a water vapor sorption (WVS) curve. The water spreading pressure, liquid-solid adhesion work and the surface energy can be extrapolated from the WVS curves[53, 54].

RDE test

All electrochemical measurements were performed using a Biological VSP potentiostat equipped with high-speed rotators (MSR-RDE-E5) from Pine Instruments (Pine Research Instrumentation, Durham, NC). A rotating disk electrode (RDE) from Pine Research Instrumentation was used as the working electrode with a glassy carbon disk: OD = 5.61 mm. A standard hydrogen reference electrode (S.H.E) ET070 (eDAQ Inc, Springs, CO) and a platinum spring counter electrode (99.99%, AFCTR5, Pine Research Instrumentation, Durham, NC) was used in a three-electrode electrochemical cell. To prepare the working electrode, 5 mg catalyst was dispersed ultrasonically in a 5 mL mixture of isopropanol and DI-water to form an ink. The ink was then drop-casted on the surface of the glassy carbon disk with a designated loading of 20 μg_{Pt} cm^{-2} and dried at room temperature to yield a uniform thin-film electrode. All the cyclic voltammetry (CV) and ORR polarization curves were recorded in 0.1 M $HClO_4$ (70 wt.%, double distilled, VERITAS, GFS Chemicals, Powell, OH, USA) and the ORR activity was measured in 0.1 M $HClO_4$ saturated with O_2 at 1600 rpm using linear sweep voltammetry (LSV) polarization plots at a scan rate of 10 mV s^{-1}.

MEA fabrication. MEA was prepared using the catalyst coated membrane (CCM) method where the catalyst ink was directly sprayed onto the proton exchange membrane (Gore® 10 μm) sitting on a hot plate at 70 °C. Active geometric area of MEA is 5 cm^2, 3.51 cm x 1.42 cm. For comparison, identical anode catalyst layers were prepared with Pt loading of 0.1 $mg_{Pt} \cdot cm^{-2}$ (±0.01) using 20wt.% Pt-XC72 (Jiping®, Shanghai, China) with 0.45 I/C ratio through same CCM method mentioned above. For the cathode, except for the catalyst difference, all conditions were the same including Pt loading, I/C ratio, and the solvents. The Pt loadings of cathode was controlled to 0.107 $mg_{Pt} \cdot cm^{-2}$ (±0.01) The MEA was assembled with Sigracet® 22BB gas diffusion layer (GDL) (SIG, Germany).

MEA testing protocols. Differential flow field cell was applied for MEA testing. MEA was tested using fuel cell testing station (850e, Scribner Associate, Southern Pines, NC) at 80 °C, 100% RH, with flow rate of anodic (H_2) and cathodic (air) in 500 standard cubic centimeter per minute (sccm) and 2000 sccm, respectively under 150 kPa_{abs} for both sides. Testing protocols from the US Department of Energy (DOE) were used. MEA was tested by scanning voltage from 0.35 V to open circuit voltage (OCV) with 50 mV/step and holding 60s for each point, the corresponding current density was taken by averaging the values in last 15 seconds. Mass activity (MA) measurement follows the DOE protocol at 80 ° C and 100 % RH under pressure of 150 kPa_{abs}. The anodic flow (H_2) and cathodic flow (O_2) are 500 sccm and 2000 sccm, respectively. The MA was obtained by holding the cell voltage at 0.6 V for 5min, then, holding voltage at 0.9V $_{iR\text{-}Free}$ for 15 min and taking the average value of current in last 5 min, which was recorded every second.

Figure 1. Schematics of the structure of the catalyst layer (**a**) on a rotating disk electrode (RDE), (**b**) in a membrane electrode assembly (MEA), (**c**) the ionomer and catalyst interface, interaction between ionomer and catalyst in catalyst ink is shown in red dash box, and (**d**) schematic of the interactions of ionomer particles and catalyst/carbon particles with positive charge (red "+" signs), pristine catalyst, and negative charge (black "-" signs), over the carbon surface, respectively; isothermal titration calorimetry (ITC) results of three carbons in the mixture of water and isopropanol with ionomer, (**e**) association constant K_A, (**f**) surface area-normalized enthalpy of binding, (**g**) entropy of binding between ionomer and three carbons, respectively.

Figure 2. Particle size distribution of catalyst inks measured using ultra-small angle X-ray scattering (USAXS) of (**a**) positively charged, blank, and negatively charged catalyst inks with ionomer, (**b**) positively charged catalyst ink with/out ionomer, (**c**) blank catalyst ink with/out ionomer, and (**d**) negatively charged catalyst ink with/out ionomer, raw and fitting data inserted. Cryo-transmission electron microscope (cryo-TEM) images of (**e**) positively charged catalyst ink, (**f**) pristine catalyst ink, and (**g**) negatively charged catalyst ink (ionomer—circled in red dash line regions and catalyst—circled in yellow dash line regions).

Figure 3. Cryo-TEM images of powder scratched from (**a, b**) NH_2 catalyst layer, (**c, d**) blank catalyst layer, and (**e, f**) SO_3H catalyst layer.

Figure 4. SEM images of catalyst layer thickness of (**a**) positively charged catalyst ink, (**b**) pristine catalyst ink, and (**c**) negatively catalyst ink; pore structure of (**d**) positively charged catalyst layer, and (**e**) negatively charged catalyst layer; 3D views of the positively charged (**f**) and negatively charged catalyst layers (**g**) after FIB/SEM slice and 3D reconstruction (pores were represented in yellow color), (**h**) mercury intrusion porosimetry results of catalyst layers from three catalysts, and (**i**) pore volume of catalyst layers of three catalysts.

Figure 5. MEA performance of the Pt/V_{NH2}, Pt/V, and Pt/V_{SO3H} catalysts ($0.1 mg_{Pt}$ cm^{-2}), (**a**) H_2-air fuel cell I-V polarization curves (hollow symbols and lines) recorded under 150 kPa_{abs} of air pressure with the cathode of the three catalysts at the flow rate of air 2000

sccm and H_2 500 sccm in a differential cell, (**b**) measured mass activity and ECSA of the Pt/V_{NH2}, Pt/V, and Pt/V_{SO3H} catalysts in MEAs, (**c**) current density at 0.6 V and 0.67 V of the Pt/V_{NH2}, Pt/V, and Pt/V_{SO3H} catalysts, (**d**) power density at 0.6 V and 0.67 V of the Pt/V_{NH2}, Pt/V, and Pt/V_{SO3H} catalysts.

Figure 6. O_2 diffusion resistance of MEA versus operating pressure of (**a**) Pt/V_{NH2}, (b) Pt/V, and (**c**) Pt/V_{SO3H} cell at the flow rate of (2 vol. % O_2 in N_2) 2000 sccm and H_2 500 sccm in a differential cell, and (**d**) O_2 diffusion resistance of the Pt/V_{NH2}, Pt/V, and Pt/V_{SO3H} catalyst MEAs at 20 % and 80 % relative humidity (RH), and the difference between them.

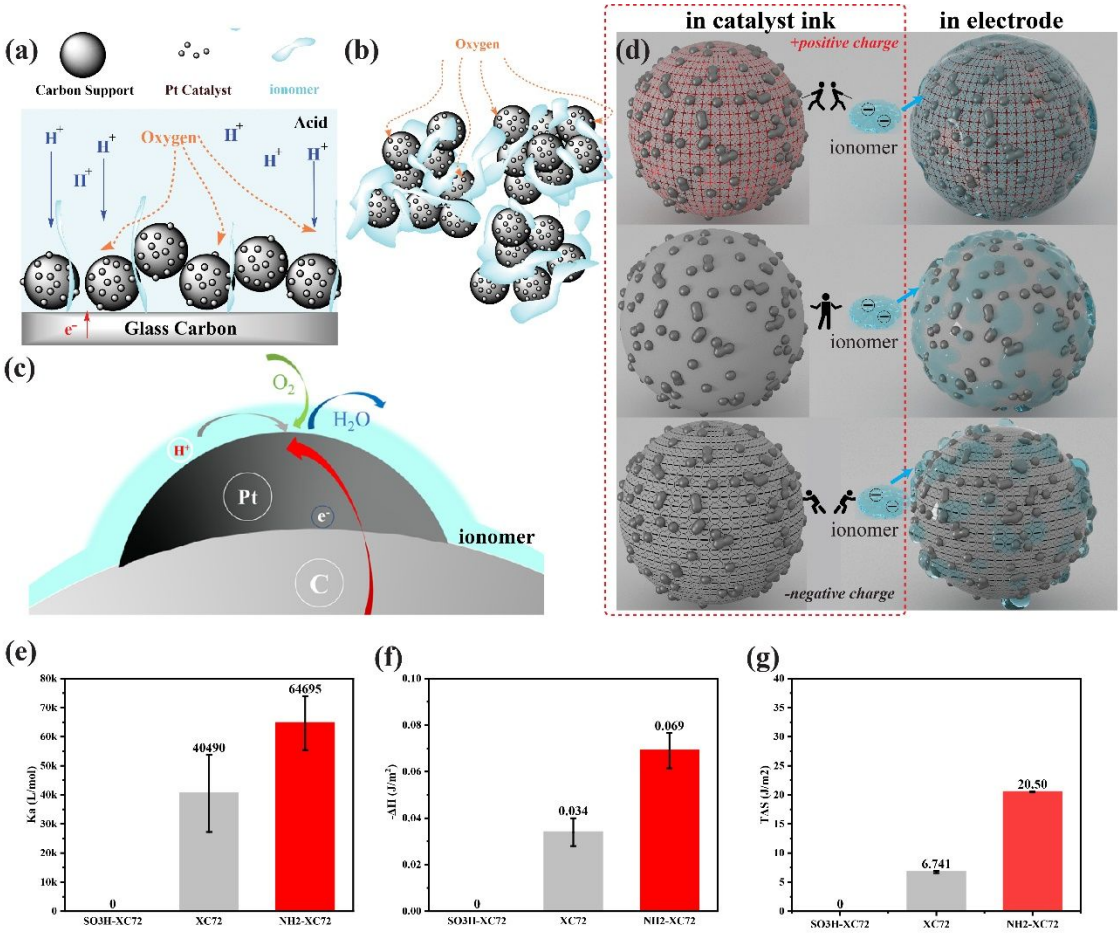

Figure.1

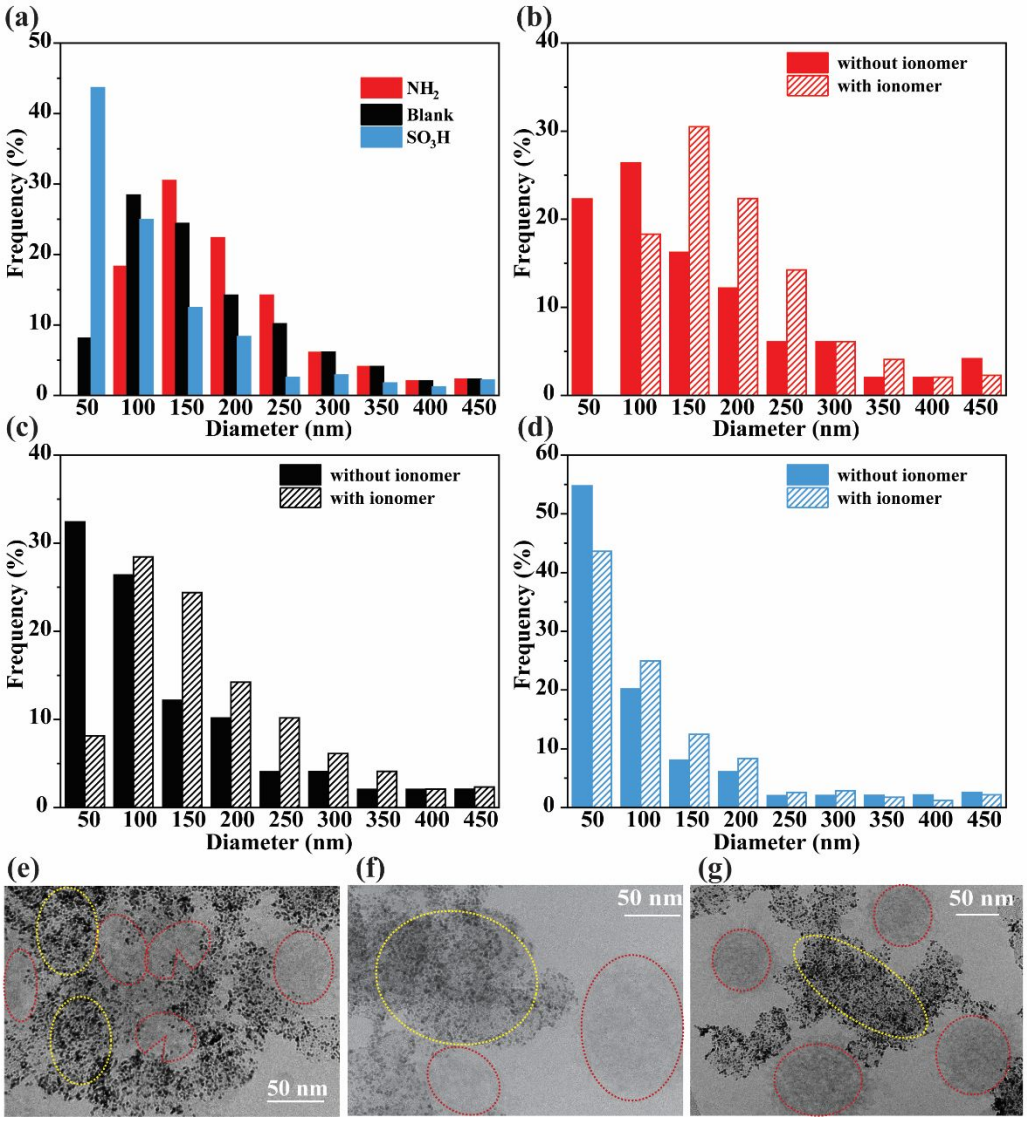
(a)
Frequency (%)
Diameter (nm)
NH2
Blank
SO3H
(b)
without ionomer
with ionomer
(c)
(d)
(e)
(f)
(g)
50 nm

Figure.2

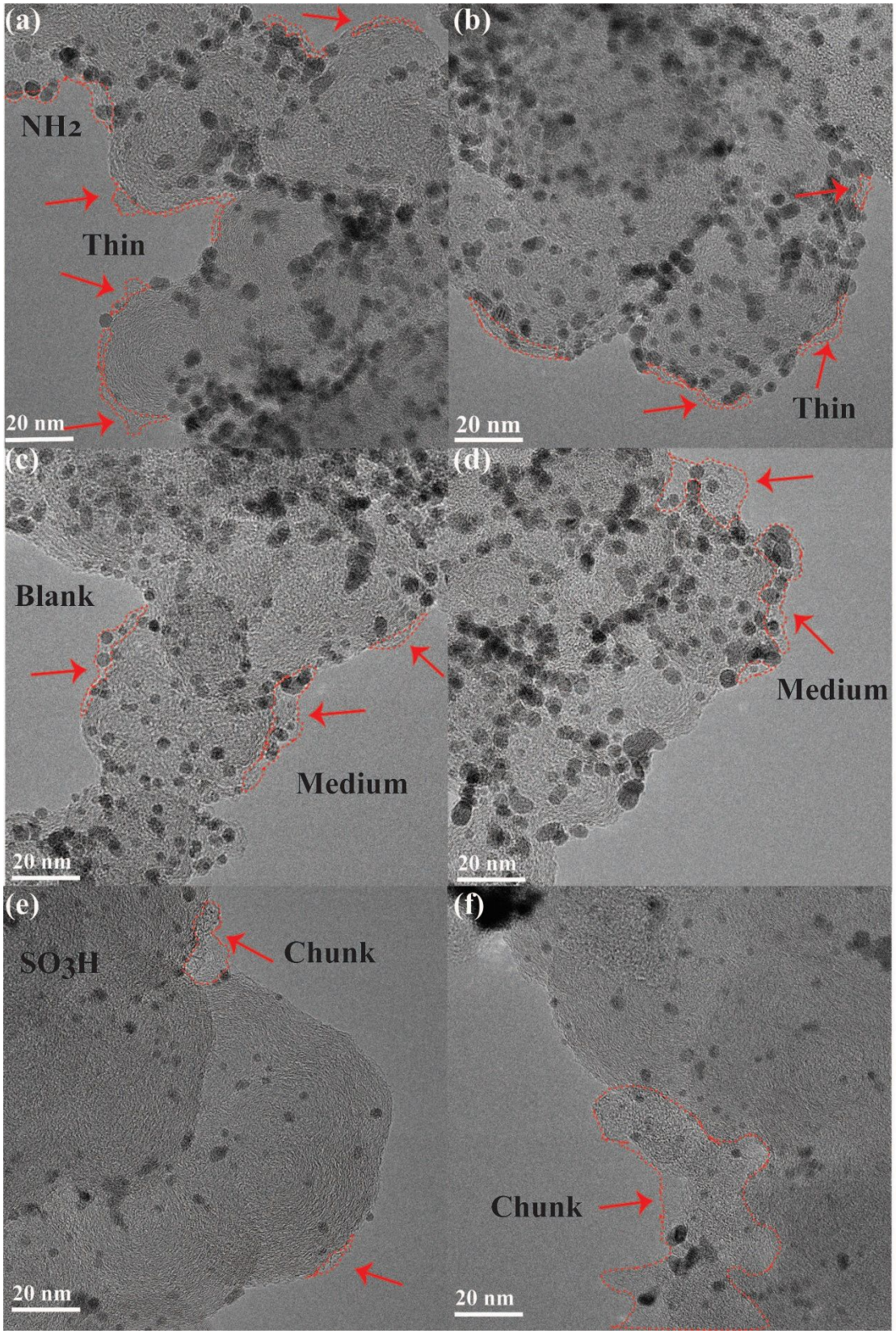
(a)
NH2
Thin
20 nm
(b)
Thin
20 nm
(c)
Blank
Medium
20 nm
(d)
Medium
20 nm
(e)
SO3H
Chunk
20 nm
(f)
Chunk
20 nm

Figure. 3

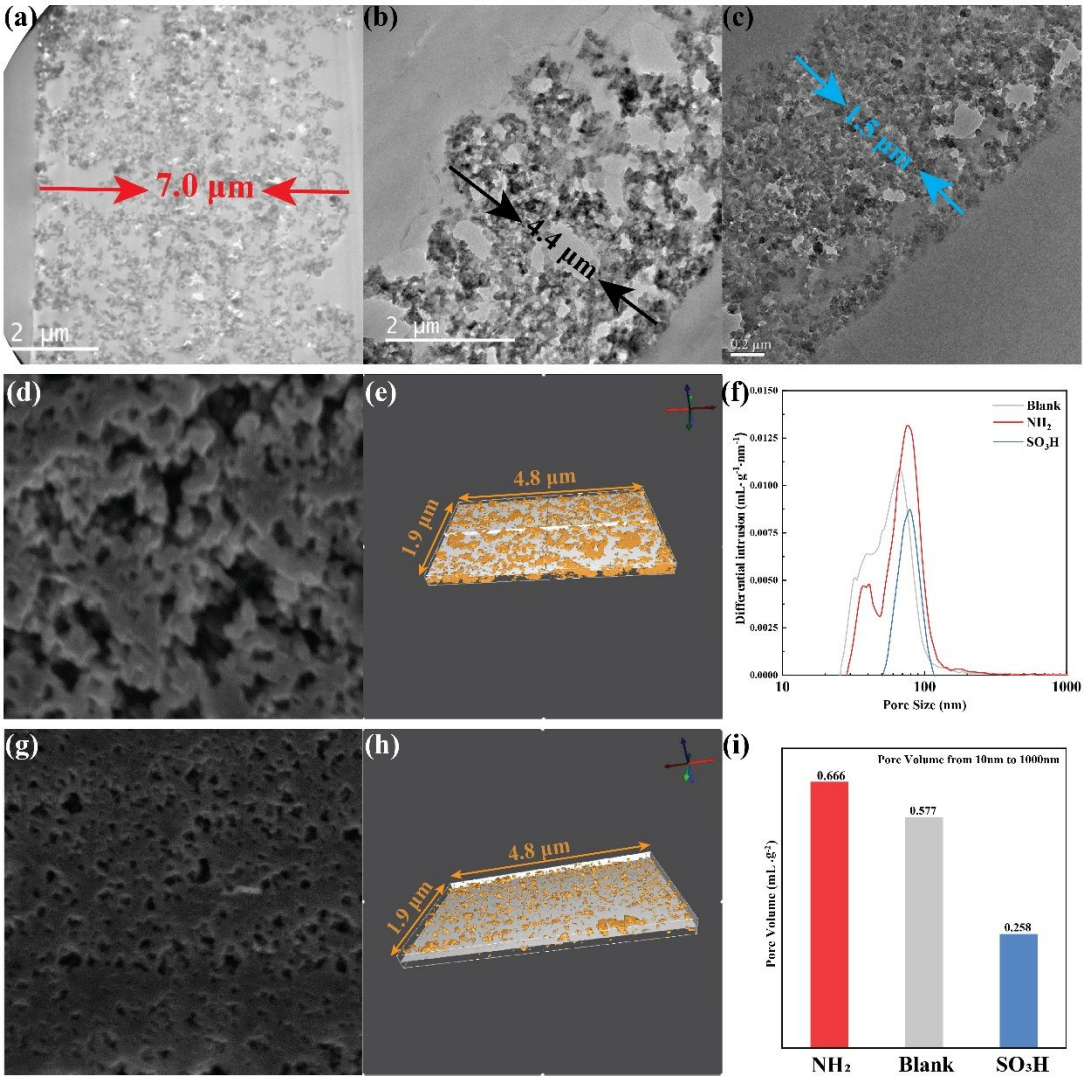
(a)
7.0 μm
2 μm
(b)
4.4 μm
2 μm
(c)
1.5 μm
0.2 μm
(d)
(e)
4.8 μm
1.9 μm
(f)
Blank
NH2
SO3H
Differential Intrusion (mL·g-1·nm-1)
Pore Size (nm)
(g)
(h)
4.8 μm
1.9 μm
(i)
Pore Volume from 10nm to 1000nm
Pore Volume (mL·g-1)
0.666
0.577
0.258
NH2
Blank
SO3H

Figure. 4

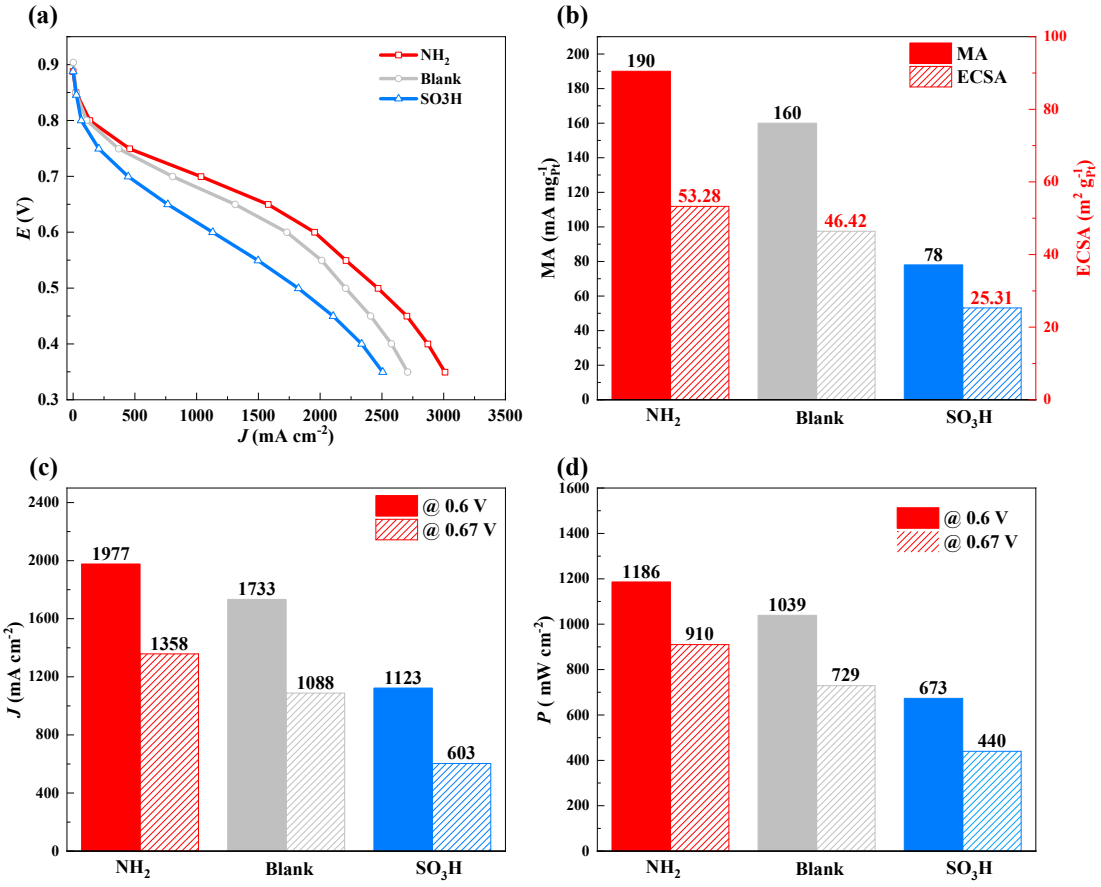
(a)
NH2
Blank
SO3H
E (V)
J (mA cm-2)
(b)
MA
ECSA
MA (mA mgPt-1)
ECSA (m2 gPt-1)
190
53.28
160
46.42
78
25.31
NH2
Blank
SO3H
(c)
@ 0.6 V
@ 0.67 V
J (mA cm-2)
1977
1358
1733
1088
1123
603
NH2
Blank
SO3H
(d)
@ 0.6 V
@ 0.67 V
P (mW cm-2)
1186
910
1039
729
673
440
NH2
Blank
SO3H

Figure. 5

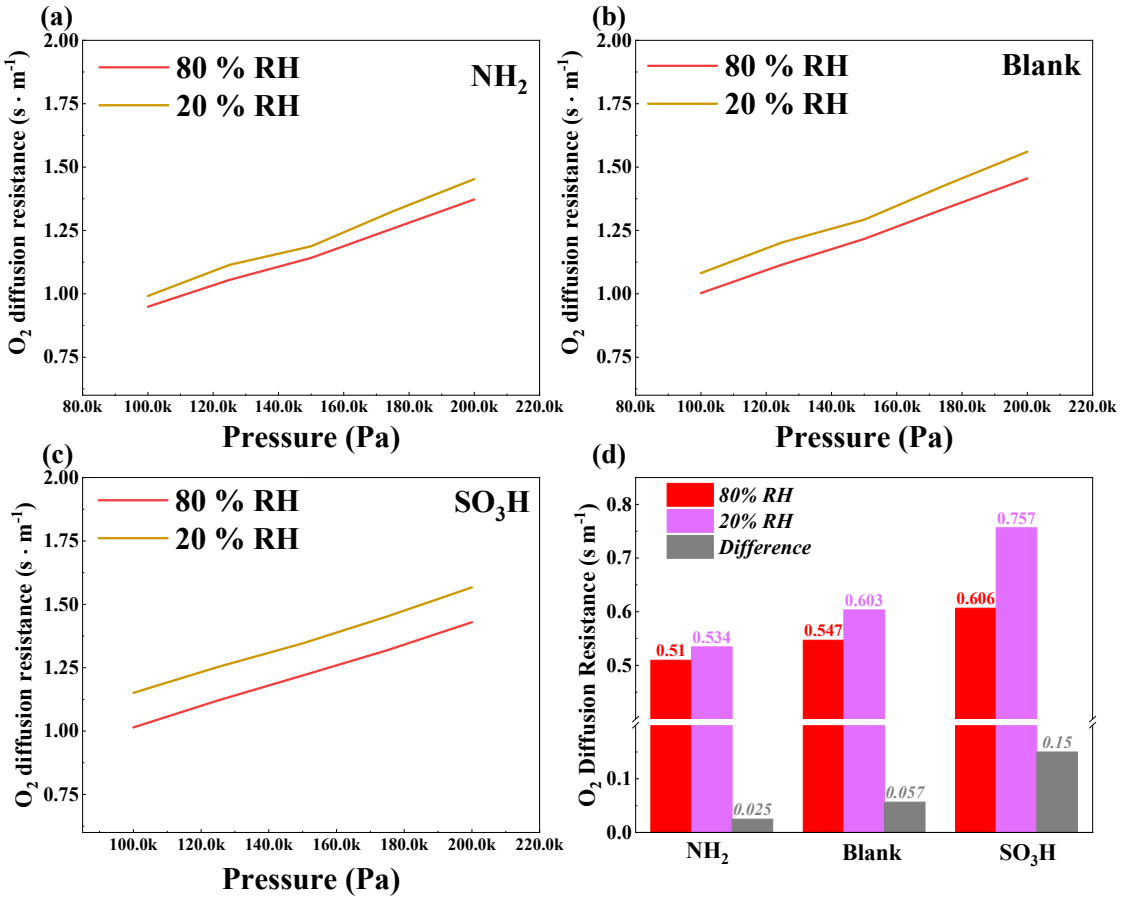

Figure. 6

Table I. Comprehensive summary of MEA polarization curve in H_2/air.

Catalyst	MA at 150 kPa (mA mg_{Pt}^{-1})	MA at 250 kPa (mA mg_{Pt}^{-1})	ECSA (m^2 g_{Pt}^{-1})	*J/P* at 0.60 V (mA cm^{-2}) (mW cm^{-2})	*J/P* at 0.67 V (mA cm^{-2}) (mW cm^{-2})
Blank	160	280	46.42	1733 (1039)	1088 (729)
NH_2	190	330	53.28	1997 (1198)	1358 (910)
SO_3H	78	130	25.31	1123 (673)	603 (440)